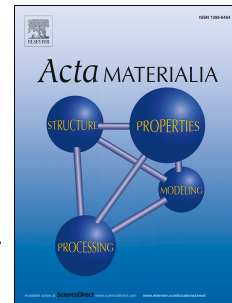


Accepted Manuscript

The effect of powder oxidation on defect formation in laser additive manufacturing

Chu Lun Alex Leung, Sebastian Marussi, Michael Towrie, Robert C. Atwood, Philip J. Withers, Peter D. Lee



PII: S1359-6454(18)30969-8

DOI: <https://doi.org/10.1016/j.actamat.2018.12.027>

Reference: AM 15035

To appear in: *Acta Materialia*

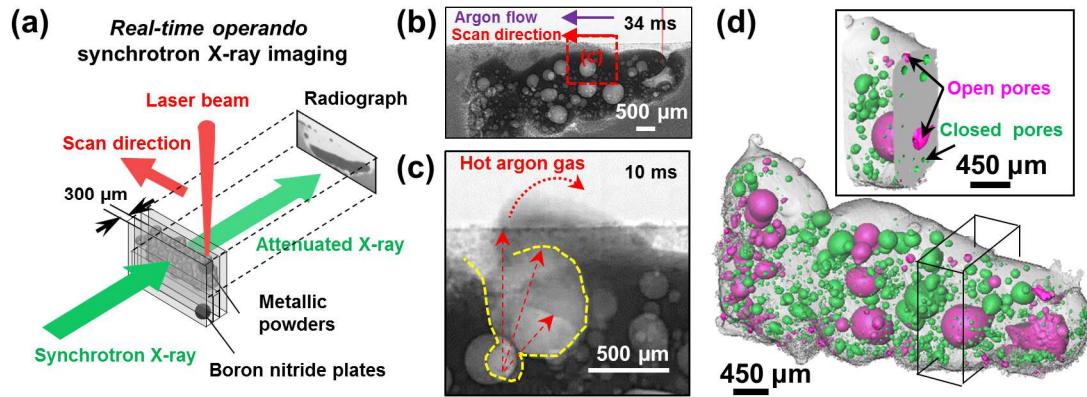
Received Date: 30 June 2018

Revised Date: 18 November 2018

Accepted Date: 12 December 2018

Please cite this article as: C.L. Alex Leung, S. Marussi, M. Towrie, R.C. Atwood, P.J. Withers, P.D. Lee, The effect of powder oxidation on defect formation in laser additive manufacturing, *Acta Materialia*, <https://doi.org/10.1016/j.actamat.2018.12.027>.

This is a PDF file of an unedited manuscript that has been accepted for publication. As a service to our customers we are providing this early version of the manuscript. The manuscript will undergo copyediting, typesetting, and review of the resulting proof before it is published in its final form. Please note that during the production process errors may be discovered which could affect the content, and all legal disclaimers that apply to the journal pertain.



1 The effect of powder oxidation on defect formation in laser additive manufacturing

2 Chu Lun Alex Leung^{1,2}, Sebastian Marussi^{2,3}, Michael Towrie⁴, Robert C. Atwood⁶, Philip J.
3 Withers³, Peter D. Lee^{1,2*}

4 ¹ Department of Mechanical Engineering, University College London, Torrington Place, London
5 WC1E 7JE, UK

6 ² Research Complex at Harwell, Rutherford Appleton Laboratory, Oxfordshire OX11 0FA, UK

7 ³ Henry Royce Institute, School of Materials, The University of Manchester, Oxford Rd, Manchester,
8 M13 9PL, UK

9 ⁴ Central Laser Facility, Research Complex at Harwell, UK Research & Innovation - Science &
10 Technology Facilities Council, Rutherford Appleton Laboratory, Oxfordshire OX11 0QX, UK

11 ⁵ Diamond Light Source Ltd, Harwell Science & Innovation Campus, Oxfordshire, OX11 0DE, UK

12 *corresponding author: peter.lee@ucl.ac.uk

13 Abstract

14 Understanding defect formation during laser additive manufacturing (LAM) of virgin, stored, and
15 reused powders is crucial for the production of high quality additively manufactured parts. We
16 investigate the effects of powder oxidation on the molten pool dynamics and defect formation during
17 LAM. We compare virgin and oxidised Invar 36 powder under overhang and layer-by-layer build
18 conditions using *in situ* and *operando* X-ray Imaging. The oxygen content of the oxidised powder was
19 found to be ca. 6 times greater (0.343 wt.%) than the virgin powder (0.057 wt.%). During LAM, the
20 powder oxide is entrained into the molten pool, altering the Marangoni convection from an inward
21 centrifugal to an outward centripetal flow. We hypothesise that the oxide promotes pore nucleation,
22 stabilisation, and growth. We observe that spatter occurs more frequently under overhang conditions
23 compared to layer-by-layer conditions. Droplet spatter can be formed by indirect laser-driven gas
24 expansion and by the laser-induced metal vapour at the melt surface. In layer-by-layer build
25 conditions, laser re-melting reduces the pore size distribution and number density either by promoting
26 gas release from keyholing or by inducing liquid flow, partially or completely filling pre-existing pores.
27 We also observe that pores residing at the track surface can burst during laser re-melting, resulting in

28 either formation of droplet spatter and an open pore or healing of the pore via Marangoni flow. This
 29 study confirms that excessive oxygen in the powder feedstock may cause defect formation in LAM.

30 Keywords: Spatter, porosity, synchrotron radiography, X-ray imaging, additive manufacturing, powder
 31 bed fusion, selective laser melting

32 **1. Introduction**

33 Laser additive manufacturing (LAM) selectively fuses powder particles together using a focused
 34 laser beam, layer-by-layer, to build up complex 3D objects [1]. It offers great promise in aerospace,
 35 nuclear fusion, and energy storage applications [2]; however, the uptake of LAM technologies in these
 36 areas has been hindered by inconsistent part performance. Specifically, the mechanical [3,4], thermal
 37 and electrical properties [5] of additive manufactured components have been lower than wrought
 38 components due to the accumulation of residual stresses [6] and the presence of defects, such as
 39 porosity [7,8], balling [9], and cracks [10].

40 Defect formation mechanisms are difficult to characterise due to the timescale of the laser-matter
 41 interaction (10^{-6} - 10^{-3} s) [11]. Although computer simulations can provide some physical understanding
 42 of the additive manufacturing (AM) processes [12], they require experimental data for model validation
 43 and verification, especially with regards to the molten pool and defect dynamics. Some data can be
 44 collected using *in situ* monitoring devices installed on AM systems [13,14]. However, these devices
 45 are unable to reveal dynamic behaviour inside the molten pool or melt track (e.g., the evolution of
 46 porosity and lack of fusion defect) while forming a single layer or multi-layer tracks. Zhao *et al.* [15]
 47 studied the molten pool dynamics and phase transformation inside a weld pool during laser powder
 48 bed fusion (LBPF) using synchrotron X-ray imaging and diffraction. Calta *et al.* [16] extended this
 49 observing pore formation and phase transformation during LBPF of a single layer track. Guo *et al.* [17]
 50 elucidated the dynamics of powder spatter during LBPF for a single layer track. Leung *et al.* [7,8]
 51 revealed and quantified defect and molten pool dynamics during LAM of single and dual-layer tracks
 52 across a wide range of overhang conditions. However, to date, there have been no *in situ* studies
 53 examining the molten pool and defect dynamics and other thermophysical phenomena taking place
 54 during LAM of virgin and oxidised powders.

55 Prior ex situ studies have shown that LAM of oxidised powder can induce defects, e.g. porosity
 56 and cracks [18–21], decrease the powder flowability resulting in poor powder packing density [22],

57 reduce the wettability of the molten pool resulting in balling [19,23], and increase the surface
 58 roughness of the part [18], impairing the overall mechanical properties [20,24]. Understanding the
 59 effects of oxygen (or oxide) in the powder feedstock on AM processes would help developing
 60 mitigation strategies to minimise defect generation when processing stored, reused and highly
 61 reactive powders, e.g. Al-, Mg- and Ti-based alloys. This is because the stored or reused powder can
 62 pick up oxygen from powder handling and the storage environment [22] while the highly reactive
 63 powders may oxidise during use. At present, it remains unclear how oxides affect the molten pool and
 64 defect dynamics and how they give rise to poor build quality.

65 Although there is a link between powder oxidation and defect formation, there are many
 66 hypotheses on the causes and formation of closed pores in AM, including 1) powder contamination
 67 [25], 2) coating defects [26,27], 3) the presence of carbon [28], hydrogen [29,30] and oxide inclusion
 68 [18] in the molten pool, 4) internal gas porosity from the powder [28,29,31], 5) keyhole collapse [32]
 69 and 6) gas entrapment during laser melting [33]. Furthermore, there are a few studies on the
 70 formation of irregular [8,18,28,34] and open pores [7,8,31]. Experiments are required to confirm the
 71 aforementioned mechanisms and to establish the conditions under which they are active.

72 Powder spatter [4,17,35,36] and droplet spatter [4,37] are two other common defects found in
 73 LAM. They influence the resultant porosity [3,31,38] and surface finish [3] of AM parts. They may also
 74 lead to powder bed contamination, improper powder spreading, and damage to the AM system.
 75 [4,39–41]

76 Powder spatter [4] contributes to powder denudation at the laser-matter interaction zone. [35] It is
 77 induced by the interactions between metal vapour and Bernoulli effect-driven gas flow, *i.e.* metal
 78 vapour-driven particle entrainment. [35,36] Bidare *et al.* [42] correlated the evolution of spatter with
 79 the direction of the metallic plume generated from LAM. Quo *et al.* [17] postulated that the amount of
 80 powder spatter increases with increasing environmental pressure and layer thickness in LBPF [7].

81 Droplet spatter can form when there is a molten pool instability due to local boiling or melt
 82 evaporation [31,43,44], accumulation of recoil pressure [4,36,45], combining with the melt flow
 83 acceleration by Marangoni convection, resulting in a stream of liquid ejecting in a vertical direction.
 84 [4,35,44–47] It can also be formed as individual powder spatter [36] or as powder agglomerates
 85 passing through the laser beam and melting [7,36].

86 Here, our aim is to find out how different levels of powder oxidation affect the AM process,
 87 including its impact on the melt pool dynamics and defect formation. To do this, we use *in situ* and
 88 operando synchrotron X-ray imaging to follow the LAM process in real time. We examine the effects
 89 of powder oxidation by studying LAM using virgin and oxidised (stored for ca. 1 year) Invar 36 powder
 90 feedstock. Our results reveal how the oxide reverses Marangoni flow, directly affecting how different
 91 types of defects form.

92 **2. Experimental methods**

93 **2.1. Powder characterisation**

94 The morphology and chemical composition of gas atomised (GA) virgin and oxidised Invar 36
 95 powder (TLS Technik GmbH & Co. Spezialpulver KG, Germany) and a virgin GA Invar 36 powder
 96 (Goodfellow Inc., UK) were characterised by a JEOL JSM-6610LV SEM equipped with energy
 97 dispersive spectroscopy (EDS). The particle size distribution was extracted using SEM images and
 98 Image Processing Toolbox in MATLAB 2016a (The MathWorks Inc, USA). X-ray Diffraction (XRD)
 99 was performed on the Invar 36 powder (TLS Technik GmbH & Co. Spezialpulver KG, Germany) using
 100 a PANalytical X'Pert Pro MPD series automated spectrometer (Malvern Instruments, UK) with a Cu_{Kα}
 101 radiation ($\lambda = 1.541\text{\AA}$) at 40kV and 40mA, a 2θ scanning range (degrees) from 10° to 100° with a step
 102 size of 0.03° , and a count rate of 50 s per step. After XRD, we performed phase identification in
 103 Profex [48]. The O, N, H, and moisture content of the virgin and oxidised Invar 36 powder was
 104 measured by an inert gas fusion infra-red absorption (IGF-IR) method (ONH836, Leco cooperation,
 105 USA). We performed the IGF-IR test on the Invar 36 powder (TLS Technik GmbH & Co.
 106 Spezialpulver KG, Germany) after second build (B2) and virgin Invar 36 powder (Goodfellow Inc., UK)
 107 as a reference powder. We performed 5 tests per powder condition and each test required 5 g of
 108 powder.

109 The chemical states of the virgin powder and oxidised powder were examined by X-ray
 110 photoelectron spectroscopy (XPS) analysis (Nexsa Surface Analysis System, Thermo Fisher
 111 Scientific Inc., USA). Both powders were characterised using a micro-focused monochromatic Al X-
 112 ray source (72 W) over an area of ca. $400 \times 400 \mu\text{m}^2$. The XPS survey was conducted at a pass
 113 energy of 200 eV with a step size of 0.1 eV and a dwell time at 10 ms. High-resolution scans were

114 conducted at a pass energy of 40 eV with a step size of 0.1eV and a dwell time of 50 ms. Charge
 115 neutralisation of the sample was achieved using a combination of low energy electrons and Ar⁺ ions.
 116 The experiment was performed at an argon partial pressure of 10⁻⁸ Torr in the x–y scan mode at
 117 ion acceleration of 3 kV and ion beam current density of 1 μA mm⁻². Binding energies were
 118 referenced to adventitious carbon at 284.8 eV, with peak fitting undertaken using CasaXPS version
 119 2.3.15 (Casa Software Ltd, UK). The multiple-peaks fitting for Fe 2p and Ni 2p high-resolution scans
 120 were assigned based on prior work from Biesinger *et al.* [49]. The overlayer thickness
 121 (oxides/hydroxide) is calculated based on the Strohmeier's equation [50]:

$$122 d = (\lambda_{avg}) \sin \theta \ln\left(\frac{N_M \lambda_M (I_{oxide} + I_{hydroxide})}{N_{avg} \lambda_{avg} I_M}\right) + 1 \text{ Equation 1}$$

123 where θ is the photoelectron take-off angle, λ_{avg} and λ_M are the average inelastic mean free path
 124 (IMPF) of the oxides/hydroxide and metal, respectively. The IMPF values (λ) were either directly
 125 obtained or calculated based on TPP-2M equation in the NIST standard reference database 71
 126 (version 1.2).[51] N_{avg} and N_M are the volume densities of the metal atoms in oxides/hydroxide and
 127 metal, respectively. I_{oxide} , $I_{hydroxide}$, and I_M are the area percentages of the oxides, hydroxide and
 128 metal from the high-resolution spectrum, respectively.

129 2.2. In situ and operando LAM with synchrotron X-ray imaging

130 To reveal the effects of powder oxide on the fluid dynamic behaviour during LAM, we compare the
 131 additive manufacture using the same Invar 36 powder in two conditions, firstly in as-supplied (low
 132 oxide condition) and secondly after storage for ca. 1 year (high oxide condition). Using a LAM process
 133 replicator (LAMPR) that can be accommodated on a synchrotron imaging beamline we perform an
 134 overhang AM build on each powder condition (for details of the LAMPR see ref [7]). In each build, the
 135 LAM process was monitored by *operando* synchrotron X-ray radiography in the Beamline I12: Joint
 136 Engineering, Environmental, and Processing (JEEP) at Diamond Light Source [52].

137 A laser beam (wavelength 1030 - 1070 nm, transverse mode TEM₀₀ - the first subscript stands for
 138 the radial mode and the second subscript stands for the angular mode of the laser beam) [11] and
 139 continuous-wave) scanned a 5 mm line at a power of 150 W and a nominal scan velocity of 5 mm s⁻¹
 140 across the Invar 36 powder bed (20 mm length, 0.3 mm wide and 3 mm deep) in an argon

141 atmosphere at a flow rate of 4 l min^{-1} . A slow scan speed (v) of 5 mm s^{-1} was chosen to ensure
142 continuous track formation under overhang conditions.

143 For the first AM build (B1), we performed LAM of a single layer track (B1.1) using a virgin Invar 36
144 powder with a 3 mm thick powder layer (for details see previous study [7]). The Invar 36 powder (TLS
145 Technik GmbH & Co. Spezialpulver KG, Germany) was then kept in a container and exposed to air
146 for ca. one year to simulate prolonged powder storage effects, allowing powder oxidation. A second
147 single layer track AM build (B2.1) was produced ca. one year after B1 using the oxidised Invar 36
148 powder under precisely the same experimental conditions as B1. In addition, we laid down second
149 (B2.2) and third (B2.3) layer melt tracks above the previous melt track while performing X-ray imaging
150 to investigate the track-to-track interaction during LAM of the oxidised powder. In this study, the
151 powder was manually spread above the substrate and melt tracks without lowering the substrate,
152 therefore the layer thickness varied depending on how the prior melt track was formed. For B2, the
153 layer thickness was ca. $3000 \mu\text{m}$, $670 \pm 420 \mu\text{m}$, and $410 \pm 170 \mu\text{m}$ for B1.1, B2.2, and B2.3,
154 receptively.

155 All experiments were captured by synchrotron X-ray radiography at 5100 frames per second (fps)
156 using 55 keV monochromatic X-rays, custom module optics with a $700 \mu\text{m}$ thick LuAg: Ce scintillator
157 coupled with a Miro 310M camera (Vision Research, USA). Using a region of interest mode, the field
158 of view (FOV) of the camera was 8.4 mm in width and 3.3 mm in height with a $6.6 \mu\text{m}$ pixel size. The
159 image acquisition system was synchronised with the LAMPR using a ring buffer mode that
160 continuously recorded images into the on-board memory of the camera. Once the laser was triggered,
161 twelve thousand radiographs were recorded. For each experiment, we also captured one hundred
162 dark-field images and one hundred flat-field images for flat field correction. [7]

163 **2.3. Post-mortem X-ray computed tomography (XCT)**

164 After the *in situ* and *operando* radiography experiments, the samples made by virgin (B1) and
165 oxidised (B2) powders were examined by X-ray computed tomography (XCT) (Nikon XTH 225 X-ray
166 microfocus tomography system, Nikon, Japan), see details in **Table 1**. The radiographic projections
167 were reconstructed into a 16-bit image volume of $2000 \times 2000 \times 2000$ voxels using the built-in beam
168 hardening correction and filtered back projection algorithms in CT Pro3D (Nikon, Japan).

169 **Table 1:** XCT acquisition parameters for the imaging of Invar 36 melt tracks.

Sample	Accelerating voltage (kV)	Beam current (μA)	Number of projections	Exposure time (ms)	Scan volume (mm^3)	Voxel size (μm^3)
B1	100	100	1200	500	7.2 ³	3.6
B2	100	100	3142	500	4.8 ³	2.4

170

171 **2.4. Image processing and quantification**

172 The acquired synchrotron radiographs were post-processed and analysed using MATLAB 2016a.
 173 They were normalized by flat field correction [53] to remove image artefacts. A denoising algorithm,
 174 VBM3D [54], was applied, followed by background subtraction and segmentation. We quantified the
 175 melt track geometry (e.g., length and depth) and its internal porosity over time (see details in [7,8]).

176 **3. Results and discussion**

177 The particle size distribution of the oxidised powder is 5 – 70 μm with a mode of 10 μm (**Figure 1**).
 178 The Inset SEM image shows the powder surface before B2 is covered with oxides (**Figure 1a**),
 179 however, it exhibits a similar morphology and shape of the virgin powder before B1 (see details in ref
 180 [7]). The XRD pattern (**Figure 1b**) is consistent with the expected face centred cubic γ -(Fe, Ni) phase.
 181 According to the Invar 36 phase diagram [55], α -(Fe, Ni) phase can be formed below 353°C [55] but it
 182 was not detected by XRD. Qiu *et al.* [56] suggested that the volume fraction of α -(Fe, Ni) phase is
 183 below the detection limit of laboratory XRD instruments. Elmer *et al.* [57] showed rapid solidification
 184 can reduce solute redistribution, resulting in a single-phase alloy. This mechanism may also apply to
 185 LAM of Invar 36, inhibiting the formation of α - (Fe, Ni) phase.

186 Given that the penetration depth of EDS is < 5 μm , the oxygen results are mainly associated with
 187 the oxide layer at the powder surfaces, therefore we removed the oxygen content and normalised the
 188 Ni and Fe contents. The EDS analysis (**Table 2**) indicate the virgin and oxidised Invar 36 powders
 189 exhibit a similar ratio of Fe and Ni content. The IGF-IR analysis (**Table 2**) was used to obtain the
 190 oxygen content from the bulk powder composition, revealing that the virgin powder (Goodfellow Inc.,
 191 UK) exhibited 6 times less oxygen than the oxidised powder due to a reduced oxide layer.

192 **Table 2:** Elemental composition of the Invar 36 powder measured by EDS and IGF-IR. The EDS
 193 results were normalised, showing a ratio of Fe and Ni content.

Characterisation method	EDS		IGF-IR			
	Fe (wt.%)	Ni (wt.%)	O (vol. %)	N (vol. %)	H (vol. %)	Moisture (ppm)
Powder sample # Virgin (B1) - TLS Technik GmbH & Co. Spezialpulver KG	69 ± 0.4	31 ± 0.4	-	-	-	-
Oxidised (B2) - TLS Technik GmbH & Co. Spezialpulver KG, Germany	71 ± 1.3	29 ± 1.3	0.343	0.666	0.00584	11.6
Virgin (Reference) - Goodfellow Inc., UK	72 ± 0.1	28 ± 0.1	0.057	0.0946	0.000915	35.9

194

195 The influence of powder surface chemistry on the molten pool dynamics is not well understood,
 196 therefore we have examined the powder surface of the virgin (reference) and oxidised invar 36
 197 powders using XPS. **Figure 2** displays high-resolution scans of Ni 2p, Fe 2p, O 1s, and C 1s from
 198 both powder samples, showing the presence of Fe, Ni, FeO, Fe₂O₃, NiO, Ni(OH)₂, and adventitious
 199 carbon contaminations.

200 From the high-resolution XPS scans of Ni (**Figure 2a** and **e**) and Fe (**Figure 2b** and **f**), the shape
 201 and the peak area percentages of metal, metal oxides, and metal hydroxides are very similar. This
 202 suggests metal oxides/hydroxide are readily formed during powder processing, including during
 203 powder packaging and powder transfer. During LAM, the metal hydroxide most likely will thermally
 204 decompose to metal oxide and then release into the melt pool. The presence of iron oxides [58] and
 205 nickel oxide [59] in the molten pool can alter its temperature coefficient of surface tension from
 206 negative to positive, leading to the reversal of the Marangoni convection, generating centripetal
 207 convection. [60]

208 Using the O 1s spectra (**Figure 2c** and **g**) and the Strohmeier's equation [50], we have estimated
 209 the thickness of metal oxides and hydroxide on both powder surfaces, *i.e.* the overlayer thickness,
 210 see **Table 3**. Unexpectedly, the overlayer of the oxidised powder is only marginally thicker than that of
 211 the virgin powder (0.5 nm, or 5% in 12 nm total). Although not captured by XPS, the reference virgin
 212 powder has a higher moisture content (**Table 2**) and formed a thick overlayer of NiO and Ni(OH)₂ at
 213 its surface. This may explain why the total overlayer thickness is similar to the oxidised powder.

214 The C 1s spectra (**Figure 2d** and **h**) also display a very similar peak shape. The total carbon
 215 contamination on the virgin and oxidised powders are 49 at.% and 17 at.%, respectively. Based on
 216 the area percentage of C 1s spectra and using the method depicted in ref. [61] the oxygen associated
 217 with the carbon species in virgin and oxidised powders were determined as 6 at.% and 15 at.%,
 218 respectively. During LAM, the carbon contaminants (containing oxygen) may either evaporate at
 219 elevated temperature or dissociate into oxygen and carbon in the molten pool. The oxygen may react
 220 with the molten Fe/Ni and form metal oxides, restricting the melt flow and promoting pore growth.

221 **Table 3:** Calculated thickness of iron oxides, nickel oxides, and nickel hydroxides

Powder type	Layer thickness (nm)				
	FeO	Fe ₂ O ₃	NiO	Ni(OH) ₂	Total
Virgin powder	1.3	7.1	1.3	2.1	11.8
Oxidised powder	1.4	8.0	1.1	1.8	12.3

222

223 3.1. LAM of virgin and oxidised Invar 36 powder

224 The initial, middle and final stages of the melt track evolution for the virgin powder (B1.1) are
 225 shown in **Figure 3a** (and complemented by **Supplementary video 1**). A high power density laser
 226 beam (10^6 W cm^{-2}) fuses the Invar 36 powder particles to form a molten pool and subsequently
 227 vaporises the top surface of the molten pool to form a metal vapour jet [17,35,36]. We postulate that
 228 the metal vapour jet indirectly heats the argon gas in the laser-matter interaction zone, both effects
 229 promote powder entrainment into the molten pool, spatter, and track growth. When the laser beam
 230 moves faster than the growth rate of the molten pool, it produces a separate molten pool ahead of the
 231 melt track. The Marangoni-driven flow and wetting move the newly formed molten pool behind the
 232 laser beam. The newly formed molten pool then merges with the melt track. [7,8] The aforementioned
 233 track formation mechanisms are summarised as molten pool wetting [7,8] and vapour-driven powder
 234 entrainment [7,36]. No pores are evident during melt track extension but spatter continues to eject
 235 from the powder bed in the same scan direction of the laser beam and argon gas flow. [7,41] Detailed
 236 quantification of the molten pool geometry and porosity during LAM is discussed in section 3.4.

237 **Figure 3 Figure 3b** and **Supplementary video 2** show the evolution of a first layer melt track for
 238 the oxidised powder (B2.1). This forms by similar mechanisms to those depicted for the virgin powder
 239 build (B1.1), however, there is extensive porosity in the first layer melt track using oxidised powder
 240 (B2.1) compared to virgin powder. In the first layer melt track with oxidised powder, the droplet spatter

241 ahead of the scanning laser beam rotates in a clockwise direction (**Figure 3b, Supplementary Figure**
242 **1** and **Supplementary video 3**). However, the pores behind the scanning laser beam move anti-
243 clockwise (**Figure 3c**), demonstrating the liquid metal in the molten pool flows radially outwards, *i.e.*
244 centripetal Marangoni convection (**Supplementary videos 2** and **3**). This is contrary to what has
245 been reported to the LAM of virgin powder study [7].

246 Most molten metals or alloys, including Fe-Ni alloys [62,63], have a negative temperature
247 coefficient of surface tension. During LAM, the flow of the liquid metal is driven by the centrifugal
248 Marangoni convection, sweeping the hotter and lower surface tension melt outwards to reduce the
249 interfacial energy of the colder and higher surface tension melt. However, some studies report that
250 when the oxygen concentration [O] in the molten pool is above 50 ppm, it is sufficient to alter the
251 temperature coefficient of surface tension from negative to positive thereby changing the Marangoni
252 convection from centrifugal to centripetal (see schematic in **Supplementary Figure 2** and
253 **Supplementary video 3**).[60,64] **Table 2** shows that the [O] of the oxidised Invar 36 powder is at
254 3430 ppm, *ca.* 6 times higher than the reference virgin Invar 36 powder. This is significantly higher
255 than the oxygen level required for centripetal Marangoni convection.

256 During LAM of oxidised powder, we observe two types of pores are present in the melt track: type
257 I – gas pores and type II – pores surrounded by oxide layers. Type I gas pores have an equivalent
258 diameter less than 250 µm, a low solubility and a high buoyancy in the melt fluid (**Figure 3c**). They
259 usually form near the laser beam and reside adjacent to the melt track surface owing to the
260 Marangoni flow. During LAM of the oxidised powder, the Marangoni flow entrains type I gas pores to
261 different locations inside the melt track via centripetal Marangoni convection. Meanwhile, some
262 coalescence occurs forming larger pores and some escape into the atmosphere via a keyhole (similar
263 observations are reported in electron beam welding [65]). Leung *et al.* [7] observed that pore bursting
264 promotes gas release from the melt track; however, the underlying mechanism remains unclear.

265 The size of the type II pores varies from 50 - 500 µm. Type II pores usually float *ca.* 200 µm
266 behind the laser beam and reside near the melt track surface. These pores remain stationary
267 throughout LAM, except for during pore growth. It is evident that the large type II pores grow at the
268 expense of type I pores via Ostwald ripening, resulting in a final pore size of at least 350 µm, see
269 examples in **Figure 3d**.

270 **3.2. Spatter evolution mechanisms**

271 From the single layer melt track experiments using virgin and oxidised powder, we observed both
 272 powder ejection and droplet spatter throughout LAM. Our results show that the laser-melt track
 273 interaction creates a laser-induced vapour jet and a recoil pressure normal to the melt track surface,
 274 ejecting powder while creating a denudation zone (**Figure 3**, **Figure 4** and **Supplementary video 3**).
 275 We speculate that the denudation zone is in an inverse bell shape and it contains a high
 276 concentration of metal vapour (**Figure 4a**). [42] The high-temperature metal vapour indirectly heats
 277 the surrounding argon gas, creating a convection or inward argon flow within the denuded zone,
 278 promoting vapour-driven powder entrainment for melt track extension [7,35,36].

279 During the overhang build, the melt track extends deeper into the powder bed while expanding in
 280 the horizontal direction, because the powder particles near the melt track are removed by the
 281 combination of metal vapour and hot argon gas. The laser beam melts the powder deeper into the
 282 powder bed and ahead of the melt track (**Figure 4a**), reducing the growth rate of the melt track as it
 283 extends. The laser beam continues to move, it eventually irradiates onto the powder ahead of the melt
 284 track and forming a new molten bead (**Figure 4b**). Sometimes, the laser beam moves ahead of the
 285 first melt bead, forming another bead whilst growing the first bead, because the laser beam profile is
 286 sufficiently broad to interact with both melt beads and the powder between the two beads. The laser
 287 beam may create a sufficiently strong vapour plume at the surface of the first bead (**Figure 4b –**
 288 **marker 1**), ejecting these new smaller metal beads (**Figure 4b – marker 2**) from the laser-matter
 289 interaction zone as droplet spatter, see examples in **Supplementary video 3**). These observations
 290 are evident in both virgin and oxidised powder cases, highlighting the difficultly of producing overhang
 291 features in LAM.

292 We have quantified the spatter size and velocity during LAM of virgin and oxidised powders, and
 293 also analysed the spatter behaviour over three different spatter size categories: (I) one; (II) one to two;
 294 and (III) > two times the powder size distribution. **Table 4** shows a similar spatter distribution in both
 295 studies wherein a majority of spatter is 1 to 2 times the particle size distribution. The oxidised powder
 296 study generates slightly more category III spatter (>132 µm) than the virgin powder study.

297 **Figure 5a** shows a positive correlation between the spatter size and velocity, although with a very
 298 large scatter. In both virgin and oxidised powder cases, most spatter has a velocity of 0.4 m s⁻¹,

however, some spatter from the oxidised powder case has a velocity in the range of $0.4 - 0.9 \text{ m s}^{-1}$. In general, the spatter velocity in both cases matches prior studies. [7,8]

Figure 5b illustrates the different spatter morphologies during LAM. With virgin powder, the spatter is roughly spherical across all size categories. With oxidised powder, the category I and II spatters are irregularly shaped and formed from agglomerated powder. It appears that the coarsening into spherical droplets is hindered, illustrating the oxides are either chemically and/or physically different. Category III spatter primarily consists of droplet spatter with its surface covered by agglomerated powder. The evidence clearly shows powder oxidation strongly affects powder agglomeration, pore formation, and pore stabilisation [66].

Table 4: Spatter tracking results for AM of virgin and oxidised powders

Size category	Spatter types	Size range (μm)	Normalised frequency (%)	
			Virgin powder	Oxidised powder
I	Powder spatter	$D_{eq} \leq 73$	3 %	4 %
II	Powder spatter/cluster + droplet spatter	$73 < D_{eq} \leq 132$	81 %	72 %
III	Droplet spatter	$D_{eq} > 132$	16 %	23 %

309

3.3. The roles of molten pool dynamics on pore bursting

In the virgin powder study, pore bursting is not evident under the processing conditions used in this study. However, Leung et al. [7] demonstrated that pore bursting occurs during solidification via pore coalescence and pore migration.

In the oxidised powder study, we have revealed a different pore bursting mechanism during LAM of the second layer melt track (B2.2) as shown in **Figure 6** and **Supplementary video 4**. The laser beam forms a keyhole, penetrating through the second powder layer and re-melting the top surface of the first layer melt track (**Figure 6a** and **Supplementary video 5**). Laser re-melting promotes pore transport in the molten pool, allowing gas pores to escape into the atmosphere through a keyhole, similar observations are shown in the first layer melt track (B2.1) and **Figure 3b**. For gas entrainment to take place, these gas pores must locate ca. 1 mm from the powder bed surface (based on our setup). Below this depth, laser re-melting can only generate a small amount of liquid metal that partially fills the pre-existing pores by liquid feeding (green dotted circles in **Figure 6a**). We speculate that the oxide films at the pore surface may act as a physical barrier, combined with the adventitious

324 carbon contaminations, altering the interfacial energy in the molten pool, restricting the melt flow that
 325 normally entrains or eliminates pores. Our observations support and validate the mechanisms
 326 proposed by previous work [18,21].

327 **Figure 6b** uncovers a new mechanism of open pore formation during LAM. At 7 ms, the laser re-
 328 melts the surface of first layer melt track and forms a liquid bridge (indicated by purple dotted lines).
 329 Between 10 and 34.8 ms, the laser beam causes the liquid bridge to double its size while accelerating
 330 its internal melt flow, which promotes pore coalescence, growth, and transport. By 34.8 ms, the
 331 Marangoni-driven flow entrains gas pores towards both ends of the liquid bridge, significantly
 332 weakening its structural integrity. The laser beam raises the temperature of the material surrounding
 333 the pore, heating the gas pore (see red dotted arrows) and expanding the volume of the gas pore
 334 proportionally. Once the gas pressure exceeds the surface tension of the liquid bridge, the liquid
 335 bridge ruptures (35 ms) and ejects vertically as a stream of liquid metal (36 ms), forming droplet
 336 spatter. Consequently, the closed pore burst opens, leaving a dent or crater (also known as an open
 337 pore [7,31,67]) at the melt track surface.

338 Based on our observations, there is no visible laser re-melting feature at the bottom of the pore
 339 until 40 ms (orange dotted circle in **Figure 6**). This indicates that the droplet spatter is ejected before
 340 the formation of an open pore, and hence metal vaporisation did not contribute to the formation of
 341 droplet spatter and open pores, an additional mechanism to prior hypotheses [35,36,42].

342 Regarding the formation mechanism of open pores, Qiu *et al.* [67] hypothesised that they are
 343 formed by insufficient liquid feeding; however, Leung *et al.* [7] revealed that open pores are formed by
 344 pore bursting during solidification. Here, we show another formation mechanism of open pores, such
 345 that pore bursting during laser melting, coupled with the formation of droplet spatter, resulting in an
 346 open pore at the track surface.

347 **Figure 7** (complemented by **Supplementary video 6**) shows the evolution of a third layer melt
 348 track (B2.3) in LAM of oxidised powder. Similar to the second layer melt track (B2.2), the laser beam
 349 melts the powder above an open pore at the front of the melt track, forming a liquid bridge which
 350 temporarily closes the pore. As LAM progresses, the laser beam induces an indirect laser-driven gas
 351 expansion inside the pore which overcomes the strength of the liquid bridge, resulting in pore bursting,
 352 followed by the formation of an open pore and droplet spatter. This repeatable observation

353 demonstrates pore bursting is a key formation mechanism of droplet spatter and open pores in LAM
 354 of oxidised powder and may apply to LAM of virgin powders. By 34 ms, the Marangoni convection
 355 causes the liquid metal to flow in the opposite direction of the scanning laser beam, showing one
 356 mechanism for pore closure. In the third layer build, laser re-melting removes many large pores in
 357 second layer melt track but also introduces many new type I pores. The oxide films at the pore
 358 surface are possibly disrupted, breaking into small pieces during laser re-melting [18]; however, they
 359 remain inside the molten pool, promoting nucleation and stabilisation of pores [68].

360 **Figure 7b** (and **Supplementary video 7**) reveals a new pore healing mechanism during LAM. The
 361 laser beam penetrates through the second and third layer melt tracks, opening a pre-existing pore
 362 (361 ms). The gas expands radially inside the pre-existing pore, pushing the liquid metal upwards
 363 (362 ms). Subsequently, the liquid metal driven by the high surface tension swirls back into the top
 364 track (indicated by dotted red arrows), healing the pore. The inward flow of liquid metal may be driven
 365 by Marangoni convection, combining with the weight of the liquid metal, causing the molten pool to
 366 swirl up and fall back down, healing the pore (361 – 363 ms).

367 Our results show that pore bursting can lead to either formation of droplet spatter resulting in an
 368 open pore (**Figure 6b**) or pore healing (**Figure 7b**). We postulate that the outcome of pore bursting
 369 depends on the size of the pre-existing pore before laser re-melting. In the third layer melt track, the
 370 diameter of the pre-existing pore is ca. 250 µm about 4 times smaller than the pore shown in the
 371 second layer build (**Figure 6b**). The gas pressure exerted from the pore in **Figure 7b** is expected to
 372 be lower than the one in **Figure 6b**. During laser re-melting, an interaction between the laser beam
 373 and a low gas pressure pore may lead to pore healing whereas the interaction between the laser
 374 beam and a high gas pressure pore may lead to the formation of droplet spatter. We also hypothesise
 375 that the position of the gas pores and the liquid bridge will affect the outcomes of pore bursting (see
 376 34.8 ms in **Figure 6b**). However, a further study is required to determine whether there are a critical
 377 pore diameter and position that lead to pore healing or formation of droplet spatter, resulting in open
 378 pore during laser re-melting.

379 **3.4. Time-resolved quantification of molten pool geometry and porosity**

380 Using the X-ray radiographs, we have quantified the changes in melt track geometry and its
 381 internal porosity throughout LAM, see **Figure 8**. **Figure 8a** shows the track length for oxidised powder

382 (L-B2.1) is ca. 20% greater than virgin powder (L-B1.1). This is due to 1) the reduced surface tension
 383 causes the molten pool to spread out further, and 2) the increased in spatter ahead of the laser beam,
 384 extending the track towards the bottom of the powder bed. The track depth in the oxidised powder
 385 study (D-B2.1) is twice of that in the virgin powder study (D-B1.1), because the reversal of Marangoni
 386 convection causes the liquid to flow inwardly from the centre to the bottom of the molten pool,
 387 advecting heat down to make a deeper pool while entraining gas pores. The entrained porosity
 388 increases the track volume and melt depth. [59]

389 **Figure 8b** quantifies porosity evolution during LAM. In the virgin powder study (blue), the molten
 390 pool/melt track continues to release gas bubbles in LAM as can be seen by the changes of greyscale
 391 in **Supplementary Video 8**. These gases are not retained in the melt track due to their low solubility,
 392 and thus the 2D porosity analysis shows the final porosity (Pore-B1.1) is 0.02%. From
 393 **Supplementary Video 8**, it is also evident that with virgin powder, the pores are driven to the surface
 394 by centrifugal Marangoni convection and then escape into the atmosphere.

395 In contrast, the melt track produced by the oxidised powder shows a large increase of porosity at
 396 the onset of the LAM (green), resulting in up to 24% final porosity (Pore-B2.1). The overlayer of
 397 oxide/hydroxide on the oxidised powder surfaces appears to have two strong effects on porosity.
 398 Firstly, this generates a centripetal Marangoni convection which drives any pre-existing pores to the
 399 bottom of the melt pool; secondly, the Marangoni convection deepens the melt pool and facilitates
 400 pore coalescence. Our results suggest the oxide stabilises the pores once formed, reduces the
 401 interfacial energy, and hence increases the pore size [69,70]. Given that the quantification algorithm
 402 does not take open pores into account, the sudden decrease of porosity in the second layer build (see
 403 event 1 in Pore-B2.2) indicates the formation of an open pore via pore bursting. In the third layer build,
 404 another drop in porosity (see event 2 in Pore-B2.3) denotes another pore bursting event has taken
 405 place. As LAM progresses, the porosity gradually decreases from 24% to 18% because laser
 406 remelting allows gas porosity to escape from the keyhole at a penetration depth of < 1 mm.

407 3.5. Post-mortem 3D analysis

408 The pixel resolution of the synchrotron X-ray imaging setup is 6.6 μm per pixel, this implies we are
 409 unable to quantify any pores with a diameter less than approximately 20 μm [71], additionally, the
 410 radiographic analysis does not consider the pore depth along the X-ray beam path. Hence, we

411 performed high-resolution XCT scans (with $2.4 \times 2.4 \times 2.4 \mu\text{m}^3$ per voxel) to examine the samples
 412 made from virgin and oxidised powders, visualising and quantifying the morphology and pore size
 413 distributions in 3D.

414 **Figure 9a** shows that the melt track produced from the virgin powder exhibits 0.08% porosity.
 415 Based on the resolution of the XCT data, the melt track shows no open pores but contains some
 416 closed pores with an area equivalent diameter (D_{eq}) of 10 μm . **Figure 9b** shows that the melt track
 417 produced from an oxidised powder has a total porosity of 15.1%, two-thirds of that (8.6%) is open
 418 pores and one-third of that (6.5%) is closed pores.

419 The largest closed pore in the sample made from virgin powder (B1) has a D_{eq} of 70 μm whereas
 420 the largest closed and open pores in the sample made from oxidised powder (B2) having a D_{eq} of 540
 421 μm and 610 μm , respectively. The normalised frequency graphs (**Figure 9c**) show that both samples
 422 exhibit a significant amount of small pores with a D_{eq} of 10 μm . We postulate that they are type I gas
 423 pores due to their small size. In contrast, the cumulative frequency graphs (**Figure 9c**) show that
 424 there are fewer and larger pores in B2 sample than those in B1 sample, suggesting that the presence
 425 of oxide films in the molten pool promotes pore formation and possibly pore growth during LAM.
 426 These pores are potent crack initiator that deteriorates the fatigue resistance of AM parts when they
 427 are under cyclic loading.[72]

428 **4. Conclusions**

429 This study addresses the effects of powder oxidation on the molten pool dynamics and reveals new,
 430 evolution mechanisms of spatter, porosity and denuded zone during LAM of virgin and oxidised
 431 powders.

432 Three types of powders were characterised by SEM-EDS, IGF-IR, and XPS, including a virgin powder
 433 for B1, an oxidised powder for B2 (same powder used for B1 but kept for 1 year), and a reference
 434 virgin powder. The oxidised powder shows an increasing of oxide layer thickness due to either oxygen
 435 pick up from powder handling and/or long-term storage under non-ideal conditions.

436 Our results confirm that molten pool wetting and vapour-driven powder entrainment are key track
 437 growth mechanisms for LAM. The oxygen content from the oxidised powder is sufficient to alter the
 438 temperature coefficient of the surface tension of the molten Invar 36 from negative to positive, altering

439 the Marangoni convection from an outward centrifugal to inward centripetal flow. The oxides may act
440 as nucleation sites for pore formation and subsequently stabilise these pores.

441 Two types of pores are revealed in the melt tracks: Type I gas pores have a diameter less than 250
442 µm, a low solubility, and a high buoyancy in the liquid metal whereas type II pores with a diameter
443 greater than 250 µm can be formed by coalescing type I pores and also promoted by the presence of
444 oxide film, stabilising the pore structure and restricting pore transport.

445 The powder surface chemistry is very complex and has impacts to powder agglomeration and defect
446 formation. In the oxidised powder study, a significant amount of spatter is evident during LAM and
447 some of which are covered by powder agglomerates, removing significant of powder in the powder
448 bed.

449 Laser re-melting under layer-by-layer conditions may disrupt the oxide layers within the prior melt
450 tracks, enabling gas pores to escape into the atmosphere via keyholing. It also reduces the size of
451 pre-existing pores if these pores are located within the laser penetration depth of ca. 1 mm for the
452 conditions studied. Otherwise, pores are partially filled by liquid feeding, changing them from a
453 spherical to an irregular shape.

454 We uncover two new phenomena associated with pore bursting during LAM: (1) promoting pore
455 healing by liquid feeding or (2) inducing open pores by the formation of droplet spatter. This
456 demonstrates droplet spatter can be formed by indirect laser-driven gas expansion inside the melt
457 track and by the laser-induced vapour jet at the melt surface.

458 The quantified results and the proposed mechanisms show defects in the additive manufacture can
459 be minimised by using a low oxygen content metal powder. The new formation mechanisms of open
460 pores and droplet spatter can enhance existing process simulation models to predict these defects.
461 The quantification of melt track geometry over time can be used to calibrate the simulation model to
462 accurately predict the fluid flow behaviour during LAM. Lastly, the porosity quantification over time can
463 be used to verify and enhance existing process simulation for defect prediction during layer-by-layer
464 build conditions.

465 **5. Acknowledgments**

466 The authors acknowledge financial support from the EPSRC MAPP Future Manufacturing Hub
 467 (EP/P006566/1, www.mapp.ac.uk) and grants (EP/I02249X/1 and EP/M009688/1) and the AMAZE
 468 (Additive Manufacturing Aiming towards Zero Waste and Efficient Production of High-Tech Metal
 469 Products) project funded by the 7th Framework Programme of the European Commission (contract
 470 FP7-2012-NMP-ICT-FoF-313781). We acknowledge the use of facilities and support provided by
 471 the Research Complex at Harwell and thank Diamond Light Source for providing the beamtime
 472 (proposal numbers: EE13641-1 and EE16214-1) and staff (including Dr. Kazimir Wanelik) at beamline:
 473 I12 for their technical assistance. We thank the team members (particularly Drs. Anne-Laure Fauchille,
 474 Enyu Guo, Daniil Kazantsev, Sam Tammas-Williams, and Miss Lorna Sinclair) for their assistance in
 475 the beam times. We would also like to thank Mr. Xiaomeng Shi for his assistance for performing
 476 powder characterisation using XRD and LPW technology Ltd. for conducting the inert gas fusion
 477 infra-red (IGF-IR) absorption tests on the virgin and oxidised Invar 36 powders. PJW is grateful for
 478 funding from the ERC Advanced Grant (CORREL-CT Project ID: 695638). XPS data collection was
 479 performed at the EPSRC National Facility for XPS ('HarwellXPS'), operated by Drs Shaoliang Guan
 480 and Mark Isaacs. From Cardiff University and UCL under contract No. PR16195.

481 **6. References**

- 482 [1] J. Bonnin Roca, P. Vaishnav, E.R.H. Fuchs, M.G. Morgan, Policy needed for additive
 483 manufacturing, *Nat. Mater.* 15 (2016) 815–818. <http://dx.doi.org/10.1038/nmat4658>.
- 484 [2] T.M. Pollock, Alloy design for aircraft engines, *Nat. Mater.* 15 (2016) 809–815.
 485 <http://dx.doi.org/10.1038/nmat4709>.
- 486 [3] C. Qiu, S. Yue, N.J.E. Adkins, M. Ward, H. Hassanin, P.D. Lee, P.J. Withers, M.M. Attallah,
 487 Influence of processing conditions on strut structure and compressive properties of cellular
 488 lattice structures fabricated by selective laser melting, *Mater. Sci. Eng. A* 628 (2015) 188–197.
 489 doi:10.1016/j.msea.2015.01.031.
- 490 [4] Y. Liu, Y. Yang, S. Mai, D. Wang, C. Song, Investigation into spatter behavior during selective
 491 laser melting of AISI 316L stainless steel powder, *Mater. Des.* 87 (2015) 797–806.
 492 doi:10.1016/j.matdes.2015.08.086.
- 493 [5] K.A. Ibrahim, B. Wu, N.P. Brandon, Electrical conductivity and porosity in stainless steel 316L
 494 scaffolds for electrochemical devices fabricated using selective laser sintering, *Mater. Des.*
 495 106 (2016) 51–59. doi:10.1016/j.matdes.2016.05.096.
- 496 [6] M. Shiomi, K. Osakada, K. Nakamura, T. Yamashita, F. Abe, Residual stress within metallic
 497 model made by selective laser melting process, *CIRP Ann. - Manuf. Technol.* 53 (2004) 195–
 498 198. <http://www.sciencedirect.com/science/article/pii/S0007850607606775>.
- 499 [7] C.L.A. Leung, S. Marussi, R.C. Atwood, M. Towrie, P.J. Withers, P.D. Lee, In situ X-ray
 500 imaging of defect and molten pool dynamics in laser additive manufacturing, *Nat. Commun.* 9

- 501 (2018) 1355. doi:10.1038/s41467-018-03734-7.
- 502 [8] C.L.A. Leung, S. Marussi, M. Towrie, J. del Val Garcia, R.C. Atwood, A.J. Bodey, J.R. Jones,
503 P.J. Withers, P.D. Lee, Laser-matter interactions in additive manufacturing of stainless steel
504 SS316L and 13-93 bioactive glass revealed by in situ X-ray imaging, *Addit. Manuf.* (2018).
505 doi:10.1016/J.ADDMA.2018.08.025.
- 506 [9] N.K. Tolochko, S.E. Mozzharov, I.A. Yadroitsev, T. Laoui, L. Froyen, V.I. Titov, M.B. Ignatiev,
507 Balling processes during selective laser treatment of powders, *Rapid Prototyp. J.* 10 (2004)
508 78–87. doi:10.1108/13552540410526953.
- 509 [10] N.J. Harrison, I. Todd, K. Mumtaz, Reduction of micro-cracking in nickel superalloys processed
510 by Selective Laser Melting: A fundamental alloy design approach, *Acta Mater.* 94 (2015) 59–
511 68. doi:10.1016/j.actamat.2015.04.035.
- 512 [11] Steen, William; Jytirmoy, Mazumder, *Laser material processing*, 4th ed., Springer-Verlag
513 London, 1998. doi:10.1007/978-1-84996-062-5.
- 514 [12] M. Markl, C. Körner, Multiscale modeling of powder bed-based additive manufacturing, *Annu.
515 Rev. Mater. Res.* 46 (2016) 93–123. doi:10.1146/annurev-matsci-070115-032158.
- 516 [13] S.K. Everton, M. Hirsch, P. Stravroulakis, R.K. Leach, A.T. Clare, Review of in-situ process
517 monitoring and in-situ metrology for metal additive manufacturing, *Mater. Des.* 95 (2016) 431–
518 445. doi:10.1016/j.matdes.2016.01.099.
- 519 [14] M. Mahesh, B. Lane, A. Donmez, S. Feng, S. Moylan, R. Fesperman, Measurement science
520 needs for real-time control of additive manufacturing powder bed fusion processes, 2015.
521 doi:dx.doi.org/10.6028/NIST.IR.8036.
- 522 [15] C. Zhao, K. Fezzaa, R.W. Cunningham, H. Wen, F. Carlo, L. Chen, A.D. Rollett, T. Sun, Real-
523 time monitoring of laser powder bed fusion process using high-speed X-ray imaging and
524 diffraction, *Sci. Rep.* 7 (2017) 3602.
- 525 [16] N.P. Calta, J. Wang, A.M. Kiss, A.A. Martin, P.J. Depond, G.M. Guss, V. Thampy, A.Y. Fong,
526 J.N. Weker, K.H. Stone, C.J. Tassone, M.J. Kramer, M.F. Toney, A. Van Buuren, M.J.
527 Matthews, An instrument for in situ time-resolved X-ray imaging and diffraction of laser powder
528 bed fusion additive manufacturing processes, *Rev. Sci. Instrum.* 89 (2018) 055101.
529 doi:10.1063/1.5017236.
- 530 [17] Q. Guo, C. Zhao, L.I. Escano, Z. Young, L. Xiong, K. Fezzaa, W. Everhart, B. Brown, T. Sun, L.
531 Chen, Transient dynamics of powder spattering in laser powder bed fusion additive
532 manufacturing process revealed by in-situ high-speed high-energy x-ray imaging, *Acta Mater.*
533 151 (2018) 169–180. doi:10.1016/j.actamat.2018.03.036.
- 534 [18] E. Louvis, P. Fox, C.J. Sutcliffe, Selective laser melting of aluminium components, *J. Mater.
535 Process. Tech.* 211 (2011) 275–284. doi:10.1016/j.jmatprotec.2010.09.019.
- 536 [19] D. Gu, D. Dai, Role of melt behavior in modifying oxidation distribution using an interface
537 incorporated model in selective laser melting of aluminum-based material, *J. Appl. Phys.* 120
538 (2016) 083104. doi:10.1063/1.4961410.
- 539 [20] E. Jelis, M. Clemente, S. Kerwien, N.M. Ravindra, M.R. Hespos, Metallurgical and Mechanical
540 Evaluation of 4340 Steel Produced by Direct Metal Laser Sintering, *JOM.* 67 (2015) 582–589.
541 doi:10.1007/s11837-014-1273-8.
- 542 [21] E.O. Olakanmi, R.F. Cochrane, K.W. Dalgarno, A review on selective laser sintering/melting
543 (SLS/SLM) of aluminium alloy powders: Processing, microstructure, and properties, *Prog.
544 Mater. Sci.* 74 (2015) 401–477. doi:10.1016/j.pmatsci.2015.03.002.
- 545 [22] J.H. Tan, W.L.E. Wong, K.W. Dalgarno, An overview of powder granulometry on feedstock
546 and part performance in the selective laser melting process, *Addit. Manuf.* 18 (2017) 228–255.
547 doi:10.1016/J.ADDMA.2017.10.011.

- 548 [23] A. Simchi, H. Pohl, Effects of laser sintering processing parameters on the microstructure and
549 densification of iron powder, *Mater. Sci. Eng. A*. 359 (2003) 119–128. doi:10.1016/S0921-
550 5093(03)00341-1.
- 551 [24] W.A. Grell, E. Solis-Ramos, E. Clark, E. Lucon, E.J. Garboczi, P.K. Predecki, Z. Loftus, M.
552 Kumosa, Effect of powder oxidation on the impact toughness of electron beam melting Ti-6Al-
553 4V, *Addit. Manuf.* 17 (2017) 123–134. doi:10.1016/j.addma.2017.08.002.
- 554 [25] B.J. Dawes, R. Bowerman, Introduction to the Additive Manufacturing Powder Metallurgy
555 Supply Chain Exploring the production and supply of metal powders for AM processes,
556 *Johnson Matthey Technol. Rev.* 59 (2015) 243–256. doi:10.1595/205651315X688686.
- 557 [26] A.B. Spierings, N. Herres, G. Levy, Influence of the particle size distribution on surface quality
558 and mechanical properties in AM steel parts, *Rapid Prototyp. J.* 17 (2011) 195–202.
559 doi:10.1108/13552541111124770.
- 560 [27] F.J. Görtler, M. Karg, M. Dobler, S. Kohl, I. Tzivilsky3, M. Schmidt, Influence of powder
561 distribution on process stability in laser beam melting: Analysis of melt pool dynamics by
562 numerical simulations, in: *Solid Free. Symp. Texas*, 2014: pp. 1099–1117.
- 563 [28] M. Rombouts, J.-P. Kruth, L. Froyen, P. Mercelis, P. Merce, Fundamentals of selective laser
564 melting of alloyed steel powders, *CIRP Ann. - Manuf. Technol.* 55 (2006) 187–192.
565 doi:[http://dx.doi.org/10.1016/S0007-8506\(07\)60395-3](http://dx.doi.org/10.1016/S0007-8506(07)60395-3).
- 566 [29] N.T. Aboulkhair, N.M. Everitt, I. Ashcroft, C. Tuck, Reducing porosity in AlSi10Mg parts
567 processed by selective laser melting, *Addit. Manuf.* 1 (2014) 77–86.
568 doi:10.1016/j.addma.2014.08.001.
- 569 [30] C. Weingarten, D. Buchbinder, N. Pirch, W. Meiners, K. Wissenbach, R. Poprawe, Formation
570 and reduction of hydrogen porosity during selective laser melting of AlSi10Mg, *J. Mater.*
571 *Process. Technol.* 221 (2015) 112–120. doi:10.1016/j.jmatprotec.2015.02.013.
- 572 [31] C. Qiu, C. Panwisawas, M. Ward, H.C. Basoalto, J.W. Brooks, M.M. Attallah, On the role of
573 melt flow into the surface structure and porosity development during selective laser melting,
574 *Acta Mater.* 96 (2015) 72–79. doi:10.1016/j.actamat.2015.06.004.
- 575 [32] H. Gong, D. Christiansen, J. Beuth, J.J. Lewandowski, Melt Pool Characterization for Selective
576 Laser Melting of Ti-6Al-4V Pre-alloyed Powder, in: *Solid Free. Fabr. Symp.*, 2014: pp. 256–267.
- 577 [33] F. Léonard, S. Tammas-williams, P.B. Prangnell, I. Todd, P.J. Withers, Assessment by X-ray
578 CT of the effects of geometry and build direction on defects in titanium ALM parts, in: *Conf. Ind.*
579 *Comput. Tomogr.*, 2012: pp. 85–93. <http://www.ndt.net/article/ctc2012/papers/91.pdf>
580 (accessed August 22, 2017).
- 581 [34] L. Thijs, J. Van Humbeeck, K. Kempen, E. Yasa, J.-P. Kruth, Investigation on the inclusions in
582 maraging steel produced by Selective Laser Melting, in: *5th Int. Conf. Adv. Res. Virtual Rapid*
583 *Prototyp.*, CRC Press, 2011: pp. 297–304. doi:doi:10.1201/b11341-48\10.1201/b11341-48.
- 584 [35] M.J. Matthews, G. Guss, S.A. Khairallah, A.M. Rubenchik, P.J. Depond, W.E. King,
585 Denudation of metal powder layers in laser powder bed fusion processes, *Acta Mater.* 114
586 (2016) 33–42. doi:10.1016/j.actamat.2016.05.017.
- 587 [36] S. Ly, A.M. Rubenchik, S.A. Khairallah, G. Guss, M.J. Matthews, Metal vapor micro-jet
588 controls material redistribution in laser powder bed fusion additive manufacturing, *Sci. Rep.* 7
589 (2017) 4085. doi:10.1038/s41598-017-04237-z.
- 590 [37] D. Wang, S. Wu, F. Fu, S. Mai, Y. Yang, Y. Liu, C. Song, Mechanisms and characteristics of
591 spatter generation in SLM processing and its effect on the properties, *Mater. Des.* 117 (2017)
592 121–130. doi:10.1016/j.matdes.2016.12.060.
- 593 [38] H. Nakamura, Y. Kawahito, K. Nishimoto, S. Katayama, Elucidation of melt flows and spatter
594 formation mechanisms during high power laser welding of pure titanium, *J. Laser Appl.* 27

- 595 (2015) 032012. doi:10.2351/1.4922383.
- 596 [39] K. Mumtaz, N. Hopkinson, Selective laser melting of Inconel 625 using pulse shaping, *Rapid*
597 *Prototyp. J.* 16 (2010) 248–257. doi:doi:10.1108/13552541011049261.
- 598 [40] M. Simonelli, C. Tuck, N.T. Aboulkhair, I. Maskery, I. Ashcroft, R.D. Wildman, R. Hague, A
599 Study on the Laser Spatter and the Oxidation Reactions During Selective Laser Melting of
600 316L Stainless Steel, Al-Si10-Mg, and Ti-6Al-4V, *Mater. Mater. Trans. A.* 46 (2015) 3842–
601 3851. doi:10.1007/s11661-015-2882-8.
- 602 [41] A. Bin Anwar, Q. Pham, Effect of inert gas flow velocity and unidirectional scanning on the
603 formation and accumulation of spattered powder during selective laser melting, *Proc. 2nd Int.*
604 *Conf. Prog. Addit. Manuf. (Pro-AM 2016).* (2016).
- 605 [42] P. Bidare, I. Bitharas, R.M. Ward, M.M. Attallah, A.J. Moore, Fluid and particle dynamics in
606 laser powder bed fusion, *Acta Mater.* 142 (2018) 107–120. doi:10.1016/j.actamat.2017.09.051.
- 607 [43] W.E. King, H.D. Barth, V.M. Castillo, G.F. Gallegos, J.W. Gibbs, D.E. Hahn, C. Kamath, A.M.
608 Rubenchik, Observation of keyhole-mode laser melting in laser powder-bed fusion additive
609 manufacturing, *J. Mater. Process. Technol.* 214 (2014) 2915–2925.
610 doi:10.1016/j.jmatprotec.2014.06.005.
- 611 [44] S.A. Khairallah, A.T. Anderson, A. Rubenchik, W.E. King, Laser powder-bed fusion additive
612 manufacturing: Physics of complex melt flow and formation mechanisms of pores, spatter, and
613 denudation zones, *Acta Mater.* 108 (2016) 36–45. doi:10.1016/j.actamat.2016.02.014.
- 614 [45] A.F.H. Kaplan, J. Powell, Spatter in laser welding, *J. Laser Appl.* 23 (2011) 032005.
615 doi:10.2351/1.3597830.
- 616 [46] V. V. Semak, J.A. Hopkins, M.H. McCay, T.D. McCay, Melt pool dynamics during laser welding,
617 *J. Phys. D. Appl. Phys.* 28 (1999) 2443–2450. doi:10.1088/0022-3727/28/12/008.
- 618 [47] A. Heider, J. Sollinger, F. Abt, M. Boley, R. Weber, T. Graf, High-speed X-ray analysis of
619 spatter formation in laser welding of copper, in: *Phys. Procedia*, 2013: pp. 112–118.
620 doi:10.1016/j.phpro.2013.03.058.
- 621 [48] N. Doebelin, R. Kleeberg, Profex: A graphical user interface for the Rietveld refinement
622 program BGNN, *J. Appl. Crystallogr.* 48 (2015) 1573–1580. doi:10.1107/S1600576715014685.
- 623 [49] M.C. Biesinger, B.P. Payne, A.P. Grosvenor, L.W.M. Lau, A.R. Gerson, R.S.C. Smart,
624 Resolving surface chemical states in XPS analysis of first row transition metals, oxides and
625 hydroxides: Cr, Mn, Fe, Co and Ni, *Appl. Surf. Sci.* 257 (2011) 2717–2730.
626 doi:10.1016/J.APSUSC.2010.10.051.
- 627 [50] B.R. Strohmeier, An ESCA method for determining the oxide thickness on aluminum alloys,
628 *Surf. Interface Anal.* 15 (1990) 51–56. doi:10.1002/sia.740150109.
- 629 [51] C.J. Powell, A. Jablonski, F. Salvat, NIST Databases With Electron Elastic-Scattering Cross
630 Sections, Inelastic Mean Free Paths, and Effective Attenuation Lengths, *Surf. Interface Anal.*
631 37 (2005). <https://www.nist.gov/publications/nist-databases-electron-elastic-scattering-cross-sections-inelastic-mean-free-paths-and> (accessed November 3, 2018).
- 633 [52] M. Drakopoulos, T. Connolley, C. Reinhard, R. Atwood, O. Magdysyuk, N. Vo, M. Hart, L.
634 Connor, B. Humphreys, G. Howell, S. Davies, T. Hill, G. Wilkin, U. Pedersen, A. Foster, N. De
635 Maio, M. Basham, F. Yuan, K. Wanekl, I2: the Joint Engineering, Environment and
636 Processing (JEEP) beamline at Diamond Light Source, *J. Synchrotron Radiat.* 22 (2015) 828–
637 838. doi:10.1107/S1600577515003513.
- 638 [53] V. Van Nieuwenhove, J. De Beenhouwer, F. De Carlo, L. Mancini, F. Marone, J. Sijbers,
639 Dynamic intensity normalization using eigen flat fields in X-ray imaging, *Opt. Express.* 23
640 (2015) 27975. doi:10.1364/OE.23.027975.

- 641 [54] K. Dabov, A. Foi, V. Katkovnik, Image denoising by sparse 3D transformation-domain
 642 collaborative filtering, *IEEE Trans. Image Process.* 16 (2007) 1–16.
 643 doi:10.1109/TIP.2007.901238.
- 644 [55] I.. V. Vernyhora, E. Al., Thermodynamics of f.c.c.-Ni–Fe Alloys in a Static Applied Magnetic
 645 Field, *ISRN Thermodyn.* 212 (2012) 917836. doi:10.5402/2012/917836.
- 646 [56] C. Qiu, N.J.E. Adkins, M.M. Attallah, Selective laser melting of Invar 36: Microstructure and
 647 properties, *Acta Mater.* 103 (2016) 382–395. doi:10.1016/j.actamat.2015.10.020.
- 648 [57] J.W. Elmer, T.W. Eagar, S.M. Allen, Single-Phase Solidification During Rapid-Resolidification
 649 of Stainless Steel Alloys, *Proc. Mater. Weldability Symp. Mater. Week*, Detroit, MI. 3 (1990)
 650 143–150.
 651 <http://citeseerx.ist.psu.edu/viewdoc/download?doi=10.1.1.666.1759&rep=rep1&type=pdf>
 652 (accessed May 2, 2018).
- 653 [58] S.-P. Lu, H. Fujii, K. Nogi, Weld shape comparison with iron oxide flux and Ar–O₂ shielding
 654 gas in gas tungsten arc welding, *Sci. Technol. Weld. Join.* 9 (2004) 272–276.
 655 doi:10.1179/136217104225012346.
- 656 [59] S. Lu, H. Fujii, H. Sugiyama, M. Tanaka, K. Nogi, Weld Penetration and Marangoni Convection
 657 with Oxide Fluxes in GTA Welding, *Mater. Trans.* 43 (2002) 2926–2931.
 658 doi:10.2320/matertrans.43.2926.
- 659 [60] K.C. Mills, B.J. Keene, R.F. Brooks, A. Shirali, Marangoni effects in welding, *Philos. Trans. R.
 660 Soc. A Math. Phys. Eng. Sci.* 356 (1998) 911–925. doi:10.1098/rsta.1998.0196.
- 661 [61] B.P. Payne, M.C. Biesinger, N.S. McIntyre, X-ray photoelectron spectroscopy studies of
 662 reactions on chromium metal and chromium oxide surfaces, *J. Electron Spectros. Relat.
 663 Phenomena.* 184 (2011) 29–37. doi:10.1016/J.ELSPEC.2010.12.001.
- 664 [62] A. Sharan, A. Cramb, Surface tension and wettability studies of liquid Fe-Ni-O alloys, *Metall.
 665 Mater. Trans. B.* 28 (1997) 465–472. doi:10.1007/s11663-997-0113-4.
- 666 [63] J. Brillo, I. Egry, Surface tension of nickel, copper, iron and their binary alloys, *J. Mater. Sci.* 40
 667 (2005) 2213–2216. doi:10.1007/s10853-005-1935-6.
- 668 [64] C.X. Zhao, C. Kwakernaak, Y. Pan, I.M. Richardson, Z. Saldi, S. Kenjeres, C.R. Kleijn, The
 669 effect of oxygen on transitional Marangoni flow in laser spot welding, *Acta Mater.* 58 (2010)
 670 6345–6357. doi:10.1016/j.actamat.2010.07.056.
- 671 [65] R.C.R. Jianglin Huang, Richard Turner, Jean-Christophe Gebelin, Nils Warnken, Martin
 672 Strangwood, The Effect of Hydrogen on Porosity Formation during Electron Beam Welding of
 673 Titanium Alloys, *Trends Weld. Res. 2012 Proc. 9th Int. Conf. (ASM Int.)* (2012) 868–875.
- 674 [66] J. Tientong, S. Garcia, C.R. Thurber, T.D. Golden, Synthesis of Nickel and Nickel Hydroxide
 675 Nanopowders by Simplified Chemical Reduction, *J. Nanotechnol.* 2014 (2014) 1–6.
 676 doi:10.1155/2014/193162.
- 677 [67] C. Qiu, N.J.E. Adkins, M.M. Attallah, Microstructure and tensile properties of selectively laser-
 678 melted and of HIPed laser-melted Ti–6Al–4V, *Mater. Sci. Eng. A.* 578 (2013) 230–239.
 679 <https://www.sciencedirect.com/science/article/pii/S0921509313005017?via%3Dihub#f0030>
 680 (accessed May 2, 2017).
- 681 [68] P.D. Lee, A. Chirazi, D. See, Modeling microporosity in aluminum-silicon alloys: A review, *J.
 682 Light Met.* 1 (2001) 15–30. doi:10.1016/S1471-5317(00)00003-1.
- 683 [69] R.C. Atwood, P.D. Lee, A three-phase model of hydrogen pore formation during the equiaxed
 684 dendritic solidification of aluminum-silicon alloys, *Metall. Mater. Trans. B.* 33 (2002) 209–221.
 685 doi:10.1007/s11663-002-0006-5.
- 686 [70] E. Guo, S. Shuai, D. Kazantsev, S. Karagadde, A.B. Phillion, T. Jing, W. Li, P.D. Lee, The

687 influence of nanoparticles on dendritic grain growth in Mg alloys, Acta Mater. 152 (2018) 127–
 688 137. doi:10.1016/J.ACTAMAT.2018.04.023.

689 [71] E. Maire, P.J. Withers, Quantitative X-ray tomography, Int. Mater. Rev. 59 (2014) 1–43.
 690 doi:10.1179/1743280413Y.0000000023.

691 [72] G. Kasperovich, J. Hausmann, Improvement of fatigue resistance and ductility of TiAl6V4
 692 processed by selective laser melting, J. Mater. Process. Technol. 220 (2015) 202–214.
 693 doi:10.1016/j.jmatprotec.2015.01.025.

694 Author contributions

695 PDL and CLAL conceived the project. CLAL, SM, and MT led the *in situ* additive manufacturing
 696 replicator and laser design. CLAL designed and performed all experiments, with all authors
 697 contributing. CLAL performed the data analysis. CLAL, PDL and PJW led the results interpretation
 698 and paper writing, with all authors contributing.

699 Data Availability

700 Representative samples of the research data are given in the figures (and supplementary data – DOI
 701 if available). Other datasets generated and/or analysed during this study are not publicly available due
 702 to their large size but are available from the corresponding author on reasonable request.

703 Competing interests

704 The authors declare no competing financial interests.

705 Figure captions

706 **Graphical abstract:** Using a laser additive manufacturing process replicator with *in situ* and
 707 *operando* X-ray imaging (a) permits capturing the formation of (b) porosity and (c) spatter during
 708 laser-matter interaction. In addition, we performed post mortem X-ray computed tomography analysis
 709 (d) reveal two types of pores inside the melt track: (i) open pores and (ii) closed pores.

710 **Figure 1:** Powder characterisation of Invar 36: (a) particle size distribution. Inset: oxygen EDS map
 711 overlaid on a SEM secondary electron image. (b) XRD pattern showing the presence of γ-phase.

712 **Figure 2:** XPS spectra of (a-d) virgin, and (e-h) oxidised Invar 36 powders. The high-resolution
 713 spectra are: (a, e) Ni 2p, (b, f) Fe 2p, (c, g) O 1s, and (d, h) C 1s.

714 **Figure 3:** Times-series radiographs showing melt features observed during LAM of the first layer
 715 Invar 36 melt track ($P = 150$ W and $v = 5$ mm s $^{-1}$) for (a) a virgin powder to form B1.1 (**supplementary**

716 (b) a oxidised (stored for ca. 1 year) powder to form B2.1 (**supplementary video 2**).
 717 Blue circle: powder spatter; red circle: molten spatter. The zoomed regions of interest (and
 718 **supplementary video 3**) in (b) two distinct pore evolution mechanisms are observed and shown in
 719 more detail in (c) pore coalescence and migration by the centripetal Marangoni convection (white
 720 arrows) and (d) pore growth promoted by oxide films (see orange circles).

721 **Figure 4:** Schematic showing the effect of laser beam position in the melt track on spatter evolution:
 722 (a) formation of powder spatter when laser beam positioned on the melt track and (b) formation of
 723 droplet spatter when the laser beam is positioned ahead of the melt track.

724 **Figure 5:** Spatter analysis for LAM of virgin and oxidised powder, divided into three categories: I.
 725 powder spatter only; II. powder spatter/agglomeration + droplet spatter; III. droplet spatter only. (a)
 726 Spatter size and velocity, and (b) spatter morphology for each category.

727 **Figure 6:** Times-series radiographs (complemented by **supplementary video 4**) showing a second
 728 layer Invar 36 melt track (B2.2) with oxidised powder ($P = 150 \text{ W}$ and $v = 5 \text{ mm s}^{-1}$). (a) Snapshots of
 729 LAM at $t = 20, 460$, and 680 ms . The red box highlights a region of interest (ROI). (b) The ROI reveals
 730 a new pore formation mechanism, where the expanded gas ejected the liquid bridge as droplet
 731 spatter (35 - 36 ms), leaving an open pore behind (40 ms) (see **supplementary video 5**). Red arrows
 732 indicate gas expansion. Purple dotted lines highlight the liquid bridge region. Orange dotted circles
 733 highlight laser re-melting at the bottom of the open pore after spattering.

734 **Figure 7:** Times-series radiographs (and **Supplementary video 6**) showing LAM of a third layer Invar
 735 36 melt track (B2.3) by a power of 150 W and a scan velocity of 5 mm s^{-1} . (a) Snapshots of the LAM
 736 process at time $t = 34, 300$ and 620 ms . (b) The ROI and **Supplementary video 7** reveal a pore
 737 healing mechanism, whereby the high surface tension of the molten pool inhibits spatter ejection,
 738 falling back to heal the pore.

739 **Figure 8:** Quantification of melt features in B2: (a) length and depth of the first (B2.1), second (B2.2),
 740 and third (B2.3) layer melt tracks and (b) the changes of porosity in each melt track over time.

741 **Figure 9:** 3D volume rendering of melt tracks made from (a) virgin powder (B1) and (b) oxidised
 742 powder (B2). (c) Their corresponding pore size distributions.

500 ms



